ChemPubSoc Europe

DOI: 10.1002/chem.201901792

CHEMISTRY
A European Journal
Full Paper

Coordination Chemistry

The First Conducting Spin-Crossover Compound Combining a Mn^{III} Cation Complex with Electroactive TCNQ Demonstrating an Abrupt Spin Transition with a Hysteresis of 50 K**

Anna V. Kazakova,*[a] Aleksandra V. Tiunova,[a, b] Denis V. Korchagin,[a] Gennady V. Shilov,[a] Eduard B. Yagubskii,*[a] Vladimir N. Zverev,[c, d] Shun Cheng Yang,[e] Jiunn-Yuan Lin,[e, f] Jyh-Fu Lee,[g] Olga V. Maximova,[b, h] and Alexander N. Vasiliev*[b, h, i]

Abstract: We present herein the synthesis, crystal structure, and electric and magnetic properties of the spin-crossover salt [Mn(5-Cl-sal-N-1,5,8,12)]TCNQ$_{1.5}$·2 CH$_3$CN (**I**), where 5-Cl-sal-N-1,5,8,12 = *N*,*N*′-bis(3-(2-oxy-5-chlorobenzylideneamino)-propyl)-ethylenediamine, containing distinct conductive and magnetic blocks along with acetonitrile solvent molecules. The Mn^{III} complex with a Schiff-base ligand, [Mn(5-Cl-sal-N-1,5,8,12)]$^+$, acts as the magnetic unit, and the π-electron acceptor 7,7,8,8-tetracyanoquinodimethane (TCNQ$^-$) is the conducting unit. The title compound (**I**) exhibits semiconducting behavior with room temperature conductivity $\sigma_{RT} \approx 1\times10^{-4}$ ohm^{-1} cm^{-1} and activation energy $\Delta \approx 0.20$ eV. In the temperature range 73–123 K, it experiences a hysteretic phase transition accompanied by a crossover between the low-spin $S=1$ and high-spin $S=2$ states of Mn^{III} and changes in bond lengths within the MnN$_4$O$_2$ octahedra. The pronounced shrinkage of the basal Mn–N bonds in **I** at the spin crossover suggests that the $d_{x^2-y^2}$ orbital is occupied/deoccupied in this transition. Interestingly, the bromo isomorphic counterpart [Mn(5-Br-sal-N-1,5,8,12)]TCNQ$_{1.5}$·2 CH$_3$CN (**II**) of the title compound evidences no spin-crossover phenomena and remains in the high-spin state in the temperature range 2–300 K. Comparison of the chloro and bromo compounds allows the thermal and spin-crossover contributions to the overall variation in bond lengths to be distinguished. The difference in magnetic behavior of these two salts has been ascribed to intermolecular supramolecular effects on the spin transition. Discrete hydrogen bonding exists between cations and cations and anions in both compounds. However, the hydrogen bonding in the crystals of **II** is much stronger than in **I**. The relatively close packing arrangement of the [Mn(5-Br-sal-N-1,5,8,12)]$^+$ cations probably precludes their spin transformation.

Introduction

Spin-crossover (SCO) phenomena can be quite varied in coordination compounds being either continuous, or abrupt with hysteresis, or even show two- or three-step transitions.[1–3] Generally, spin-state transitions are triggered by various external stimuli, for example, temperature, pressure, magnetic field, or illumination. In any case, the alteration of the spin state is accompanied by changes in the local environment of the metal, which are mostly 3d transition-state metals with a population of the d shell ranging from d^4 to d^7. The intra-atomic electron transfer influences only the magnetic and optical properties of the coordination compounds, leaving the conductive properties unaffected. This is in contrast to some inorganic systems in which spin crossover can be associated with metal/insulator transformation. For example, LaCoO$_3$ presents a two-step tran-

---

[a] Dr. A. V. Kazakova, A. V. Tiunova, Dr. D. V. Korchagin, Dr. G. V. Shilov, Prof. E. B. Yagubskii
Institute of problems of Chemical Physics, RAS
Chernogolovka, 142432 (Russia)
E-mail: kazakova@icp.ac.ru
yagubski@gmail.com

[b] A. V. Tiunova, Dr. O. V. Maximova, Prof. A. N. Vasiliev
Lomonosov Moscow State University, Moscow 119991 (Russia)
E-mail: anvas2000@yahoo.com

[c] Dr. V. N. Zverev
Institute of Solid State Physics, RAS, Chernogolovka 142432 (Russia)

[d] Dr. V. N. Zverev
Moscow Institute of Physics and Technology, Dolgoprudnyi 141700 (Russia)

[e] S. C. Yang, Prof. J.-Y. Lin
Institute of Physics, National Chiao Tung University, Hsinchu 30010 (Taiwan)

[f] Prof. J.-Y. Lin
Center for Emergent Functional Matter Science
National Chiao Tung University, Hsinchu 30010 (Taiwan)

[g] Dr. J.-F. Lee
National Synchrotron Radiation Research Center, Hsinchu 30076 (Taiwan)

[h] Dr. O. V. Maximova, Prof. A. N. Vasiliev
National University of Science and Technology "MISIS"
Moscow 119991 (Russia)

[i] Prof. A. N. Vasiliev
National Research South Ural State University, Chelyabinsk 454080 (Russia)

[**] TCNQ = 7,7,8,8,-tetracyanoquinodimethane.

Supporting information and the ORCID identification number(s) for the author(s) of this article can be found under: https://doi.org/10.1002/chem.201901792.

sition in which the spin state in Co^{III} changes from low spin (LS) $S=0$ to intermediate spin (IS) $S=1$ at about 100 K, and from the IS state to high spin (HS) $S=2$ at about 500 K, the latter being accompanied by metallization.[4]

Recently, considerable efforts have been made to synthesize molecular systems that combine enhanced conductivity with spin crossover, albeit in different segments of the crystal lattice.[5] The conductivity in these systems is secured by itinerant carriers in organic layers, whereas the layers of magnetic counter ions are considered insulating. The electron acceptors or donors in the charge-transfer systems must be available in fractional reduction or oxidation states to promote the enhanced conductivity. Thus, 7,7,8,8,-tetracyanoquinodimethane (TCNQ) would be suitable for this purpose.[6–10] The cross effects between conductivity and spin crossover are presumed due to the chemical pressure that the coordination compounds experience upon LS/HS transformation. The majority of known examples that exhibit HS/LS transitions feature six-coordinated Fe^{II} or Fe^{III} complexes, because the spin-crossover effect is most pronounced in d^5 and d^6 systems in which two electrons switch between t_{2g} and e_g orbitals.[1–3] Much rarer are the spin-state transitions in d^4 systems, represented by Mn^{III} and Cr^{II} complexes, in which one electron is transferred between t_{2g} and e_g orbitals. Mn^{III} is a particularly interesting candidate for SCO as it has a pronounced Jahn–Teller (JT) effect in the HS state. In the last decade, hexacoordinated $(N_4(O^-)_2)$ Mn^{III} cation complexes with the sal-N-1,5,8,12 Schiff-base ligand L (Scheme 1) and its derivatives have been actively studied as SCO systems.[11–21] This ligand is a product of the condensation reaction between salicylaldehyde and a flexible *N*,*N*′-bis(3-aminopropyl)ethylenediamine.

It is known that hexadentate Schiff-base ligands with a *cis*-O,O (N_4O_2) donor set usually stabilize Mn^{III} in its HS state in which axial elongation of the Mn–O and Mn–N bonds is observed due to the JT effect.[11,22] The use of an extended flexible link in the ligand L orients the phenolate oxygen atoms in a *trans* position relative to each other (Scheme 1). This gives rise to a marked Jahn–Teller distortion (axial compression of Mn–O bonds), which has a dramatic effect on the spin state of the Mn^{III} complex and as a result promotes thermal SCO.[11,12,16] Current research on this class of Mn^{III} SCO compounds is aimed at tuning the Mn^{III} spin state by varying the substituents on the phenolate ring, the anion, and the co-crystallized solvent molecules.[11–21] However, it should be noted that the vast majority of Mn^{III} SCO complexes with the ligand L and its derivatives show a gradual and often incomplete SCO. To the best of our knowledge, only three manganese complexes are known, and these exhibit abrupt SCO behavior with hysteresis windows of 8, 14, and 18 K.[15,19,21] SCO systems with wide hysteresis loops attract considerable attention, because they have great potential for practical applications in memory devices.[23] In the present work, we have used the electroactive TCNQ for the first time as the counter ion in Mn^{III} complexes formed with the sal-N-1,5,8,12 ligand family and synthesized two isomorphic semiconducting compounds, namely [Mn(5-Cl-sal-N-1,5,8,12)]TCNQ$_{1.5}$·2 CH$_3$CN (**I**) and [Mn(5-Br-sal-N-1,5,8,12)]TCNQ$_{1.5}$·2 CH$_3$CN (**II**). Complex **I** shows an abrupt spin-crossover transition with a record hysteresis width of 50 K with $T_c^{\downarrow}=73$ K and $T_c^{\uparrow}=123$ K, whereas complex **II** evidences no spin-crossover phenomena. Both the molecular and supramolecular aspects underlying the fundamental differences in the spin behavior of these compounds have been analyzed.

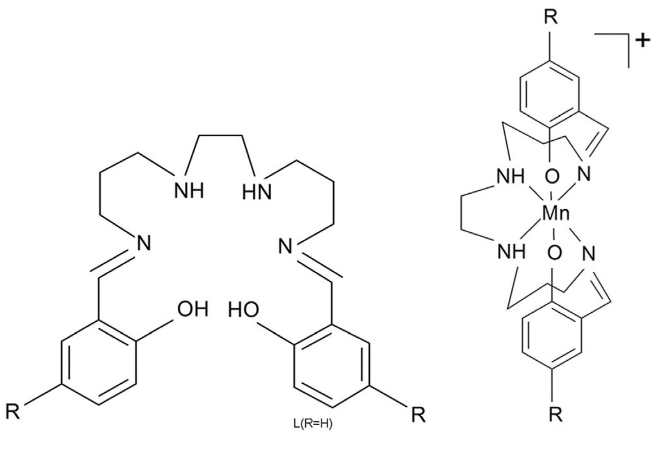

Scheme 1. Schematic view of the ligands L (R=H), L1 (R=Cl), and L2 (R=Br), and the complexes [Mn(5-R-sal-N-1,5,8,12]$^+$.

Results and Discussion

Synthesis

The compounds [Mn(5-Cl-sal-N-1,5,8,12)]TCNQ$_{1.5}$·2 CH$_3$CN (**I**) and [Mn(5-Br-sal-N-1,5,8,12)]TCNQ$_{1.5}$·2 CH$_3$CN (**II**) were obtained by a mixing hot acetonitrile solution of [Mn(5-Cl-sal-N-1,5,8,12)]ClO$_4$ or [Mn(5-Br-sal-N-1,5,8,12)]ClO$_4$ with a hot solution of LiTCNQ and TCNQ in CH$_3$CN under argon. The resulting solutions were left to stand in a refrigerator overnight and black plate-like crystals of **I** and **II** were formed (see the Experimental Section). Figures S1 and S2 in the Supporting Information display the thermograms of **I** and **II**. With increasing temperature, weight losses of 8.55 and 8.29 % are observed in the temperature range 70–150 °C with endothermic peaks at 129.2 and 149.6 °C, respectively, which have been assigned to the loss of lattice acetonitrile molecules (calcd 9.19 % for **I** and 8.35 % for **II**). In the mass spectrum of **II** recorded in the gas phase (see Figure S2), peaks are observed at *m*/*z* 41 from CH$_3$CN molecules and at *m*/*z* 15 (CH$_3$) and 26 (CN) from their fragments. On heating above 150 °C, the complexes begin to decompose (differential scanning calorimetry peak at 205 °C) with the release of CN fragments (*m*/*z* 26) from TCNQ. It should be noted that the crystals of **I** and **II** gradually lose lattice solvent during storage. Therefore, for X-ray diffraction analysis, they were kept in contact with the mother liquor.

Crystal structure

Both compounds **I** and **II** crystallize in the triclinic space group $P\bar{1}$ with one and a half TCNQ molecules per [MnL1]$^+$ or [MnL2]$^+$ complex cation and two solvent acetonitrile molecules, as shown in Figure 1. One of the TCNQ molecules occu-

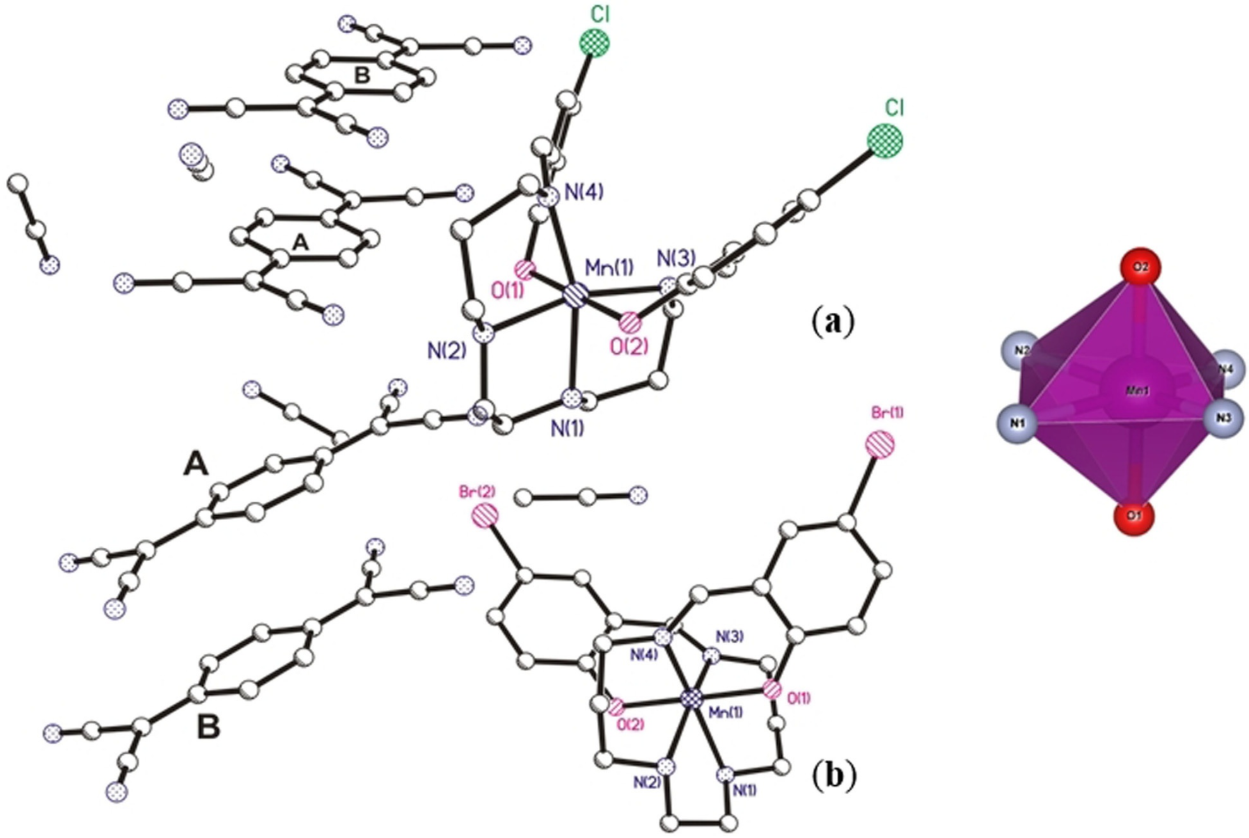

Figure 1. Molecular structures of: a) **I**, and b) **II**. Hydrogen atoms are omitted for clarity. The structure of the coordination polyhedron in the Mn cations is shown on the right.

pies a special position, that is, a center of symmetry, so there are only two independent TCNQ molecules, denoted as **A** (in a general position) and **B** (at the center of symmetry).

The structures of the complex cations $[MnL1]^+$ and $[MnL2]^+$ in compounds **I** and **II**, respectively, are almost the same and correspond to the structures of Mn^{III} cationic complexes with similar polydentate ligands.[11,13,17] The bond lengths Mn–X (X = O, N) and distortion parameters Σ (indicating the deviation from the perfect octahedral environment, a perfectly octahedral complex has $\Sigma = 0$) for the coordination polyhedra $Mn^{III}N_4O_2$ of **I** at 100 and 220 K and **II** at 100 K are listed in Table 1. The coordination geometry around manganese is a distorted square bipyramid with pronounced compression along the O(1)–Mn(1)–O(2) bonds, with the Mn–O bond lengths being similar (see Table S1 in the Supporting Information). Unlike the axial Mn–O bonds, the equatorial Mn–N bond lengths differ markedly: The Mn(1)–N_{am} bonds are longer than the Mn(1)–N_{im} bonds (2.222(3)–2.166(3) vs. 2.141(3)–2.089(3) Å for **I** at 100 K and 2.215(4)–2.175(5) vs. 2.137(4)–2.095(5) Å for **II** at 100 K). The average value of the Mn(1)–N_{eq} bonds is 2.15 Å, which significantly exceeds the average axial bond length of Mn(1)–O_{ax} of 1.88 Å.

The X–Mn(1)–X angles, except for the almost linear (179.5°) O(1)–Mn(1)–O(2) angle, significantly deviate from the ideal values of 90 and 180° and lie in the ranges 80.7(1)–109.0(1) and 164.0(1)–164.2(1)° for **I**. In the structure of **II**, the angles in the coordination polyhedron of $Mn^{III}N_4O_2$ deviate somewhat more and fall in the ranges 79.6(2)–109.7(2) and 163.1(2)–163.5(2)° (see Table S1 in the Supporting Information). The bond lengths and angles in the Mn^{III} fragments of compounds **I** and **II** are in good agreement with those in other HS Mn^{III} cation complexes bearing ligands of the sal-N-1,5,8,12 family.[11–21]

Table 1. Selected bond lengths [Å] and distortion parameter Σ [°] for the complex cations $[MnL1]^+$ and $[MnL2]^+$ of compounds **I** and **II**.

Bond	Compound **I** 100 K	 220 K	Compound **II** 100 K
Mn(1)–O(1)	1.884(2)	1.881(2)	1.886(4)
Mn(1)–O(2)	1.872(2)	1.871(2)	1.871(4)
Mn(1)–N(1)	2.222(3)	2.220(2)	2.215(4)
Mn(1)–N(2)	2.166(3)	2.172(2)	2.175(5)
Mn(1)–N(3)	2.089(3)	2.095(2)	2.095(5)
Mn(1)–N(4)	2.141(3)	2.144(2)	2.137(4)
Σ[a]	65.58(8)	66.81(6)	67.0(2)

[a] $\Sigma = \sum_{i=1}^{12}|90-\varphi_i|$ in which φ_i represent the 12 X–Mn–X (X = O, N) angles for Mn^{III}.

The overall crystal structure of compound **I** (and **II**) can be described as consisting of zigzag-like layers formed of $[MnL1]^+$ (and $[MnL2]^+$) cations and MeCN solvent molecules lying in the crystallographic *ab* plane. Adjacent cationic zigzag-like layers are slightly displaced along the *b* direction. As a result, channels parallel to the *a* axis are formed in which isolated stacks of anionic TCNQ are situated, as shown in Figure 2.

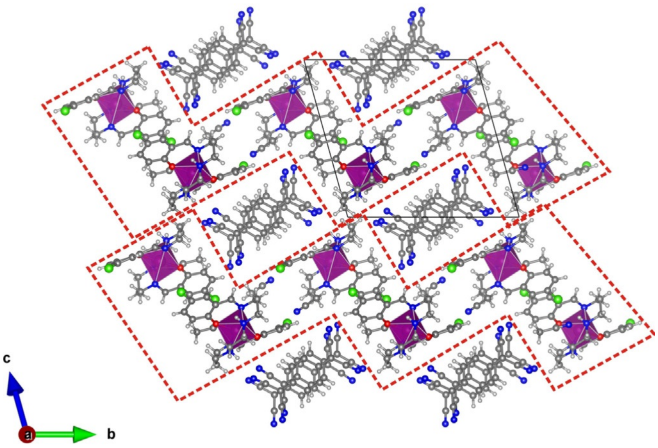

Figure 2. Fragment of the crystal structure of **I** (projection onto the *bc* plane). The dashed red lines show the cationic $[MnL1]^+$ layers.

The cationic layers are connected to each other only through TCNQ molecules by means of N(2)–H···N(10) hydrogen bonds (see Table 2) and N(8)···C(19) van der Waals contacts of 3.19 Å (3.18 Å, here and elsewhere in the text, the values for **II** are given in parentheses; Figure 3a).

In the crystal structure of **I**, the TCNQ anions are packed in isolated stacks along the *a* direction with almost equal **A**···**A** and **A**···**B** interplane separations of 3.25(3.22) and 3.26(3.26) Å, respectively (Figure 3b). The shortest C···C contact distances between two adjacent **A** molecules lie in the range 3.23(3.24)–3.37(3.37) Å, and between two adjacent **A** and **B** molecules, 3.29(3.30)–3.40(3.40) Å. Analysis of the bond lengths in the TCNQ molecules reveals strong charge localization in the stacks: The **A** molecules have a charge close to −1, whereas the **B** molecules are almost neutral. A similar charge distribution is observed in the two independent TCNQ molecules in the crystal structure of **II** (Table 3).

Previously it has been shown that the charge state of TCNQ can be estimated from its carbon–carbon bond lengths. By using the Kistenmacher relationship,[24] $\delta = M[c/(b+d)] + N$ (δ is the total charge of TCNQ species, $M = -41.667$, $N = 19.833$, and *c*, *b*, and *d* are the average bond lengths of TCNQ shown in Table 3), we estimated the charge distribution for the **A** and **B** TCNQ anions in the stacks (−0.8 and −0.2, respectively, Table 3).

These values point to different degrees of charge acceptance by the TCNQ anions. The total charge on the various TCNQ species is −1.0, which is in agreement with the +1 charge on the $[MnL1]^+$ cation. The same charge distribution is observed in the isomorphic compound **II** (Table 3).

It should also be noted that the mode of overlap of **A**···**A** and **A**···**B** in the stacks is different (see Figure S3 in the Supporting Information): The **A** molecules are arranged one above the other and completely overlap, whereas molecules **A** and **B** are displaced relative to each other in a longitudinal direction (the rings overlap the external bonds).

Table 2. Geometric parameters of the hydrogen bonds in the crystal structures of **I** and **II**.

	D–H	*d*(D–H) [Å]	*d*(H···A) [Å]	<DHA [°]	*d*(D···A) [Å]	A
I	N(1)–H(1)	0.843	2.700	170.0	3.533	Cl(2) [−*x*+1, −*y*, −*z*+3]
	N(2)–H(2)	0.882	2.205	153.7	3.022	N(10)
II	N(1)–H(1)	0.926	2.642	174.1	3.564	Br(2) [−*x*−1, −*y*, −*z*+1]
	N(2)–H(2)	0.995	2.082	150.6	2.989	N(10) [−*x*, −*y*, −*z*+2]

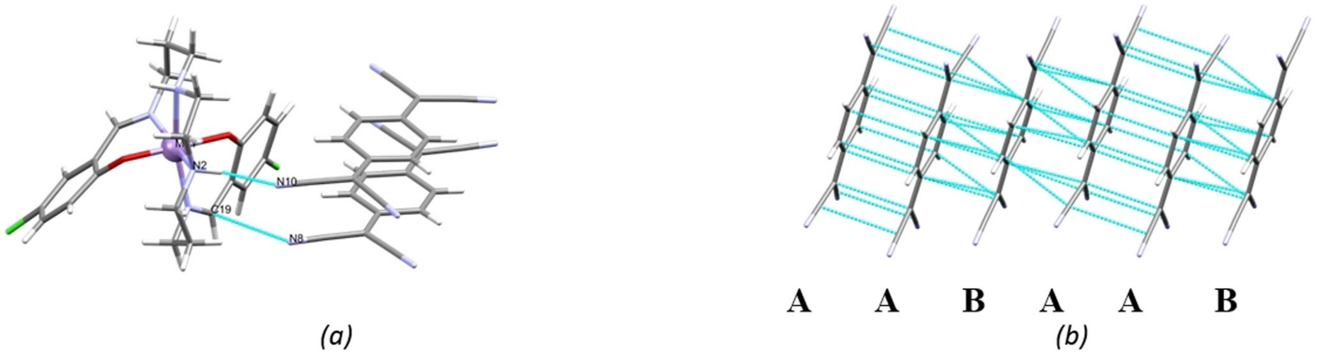

(a)

(b)

Figure 3. a) Shortest intermolecular contacts between the $[MnL1]^+$ cations and TCNQ molecules in the crystal structure of **I**. b) Stacking interactions in the anionic columns (projection onto the *ab* plane). The dashed lines show the shortest C···C contacts.

Table 3. Charges δ of different TCNQ anions in complexes **I** and **II** estimated from Kistenmacher's empirical formula.

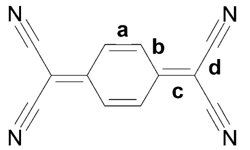

Species	*a* [Å]	*b* [Å]	*c* [Å]	*d* [Å]	*c*/*b*+*d*	δ, ē
$TCNQ^{0}$	1.346	1.448	1.374	1.440	0.476	0.0[24]
$TCNQ^{-0.5}$	1.354	1.434	1.396	1.428	0.488	−0.5[24]
$TCNQ^{-1}$	1.373	1.423	1.420	1.416	0.500	−1.0[24]
TCNQ (**I**, **A**)	1.366	1.422	1.414	1.427	0.496	−0.8
TCNQ (**I**, **B**)	1.350	1.440	1.384	1.442	0.480	−0.2
TCNQ (**II**, **A**)	1.351	1.423	1.408	1.426	0.494	−0.8
TCNQ (**II**, **B**)	1.344	1.445	1.363	1.441	0.472	−0.2

In the layers, the $[MnL1]^{+}$ cations connect to form centrosymmetric hydrogen-bonded dimers (Figure 4a). The geometric parameters of the hydrogen bonds in the crystal structures of **I** and **II** are presented in Table 2.

When comparing **I** (Cl) and **II** (Br), it can be seen that the intermolecular distances are almost the same (Table 2), which should significantly increase the energy of the hydrogen bonds in the second compound. Further small stabilization within the dimers can be provided by an offset π–π stacking interaction between the phenyl rings. Moreover, in the case of compound **II**, the interplanar distances between the phenyl rings in the dimers are slightly less (3.48 Å) than in the case of compound **I** (3.50 Å). The interconnections between adjacent dimeric units lying in the same layer are provided by short contacts with solvent molecules MeCN (Figure 4b). In the *b* axis direction, the hydrogen-bonded dimers are linked by weak C–H···H–C noncovalent contacts between the propyl and phenyl fragments of the ligands of adjacent $[MnL1]^{+}$ or $[MnL2]^{+}$ cations, as shown in Figure 4c. It should be noted that in compound **II**, these H···H contacts are somewhat shorter (2.15 vs. 2.28 Å), which also indicates an increase in the crystal-packing energy in this compound compared with in the isostructural compound **I**.

Thus, X-ray diffraction analysis of **I** and **II** showed that the structure of the coordination polyhedron $Mn^{III}N_4O_2$ in the cation fragments of these compounds is almost identical, and the compounds themselves remain in a high-spin state upon cooling to 100 K. However, the supramolecular structures of **I** and **II** are noticeably different. The hydrogen-bonding between cations and cations and anions in the crystal lattice of **II** is stronger than in **I**.

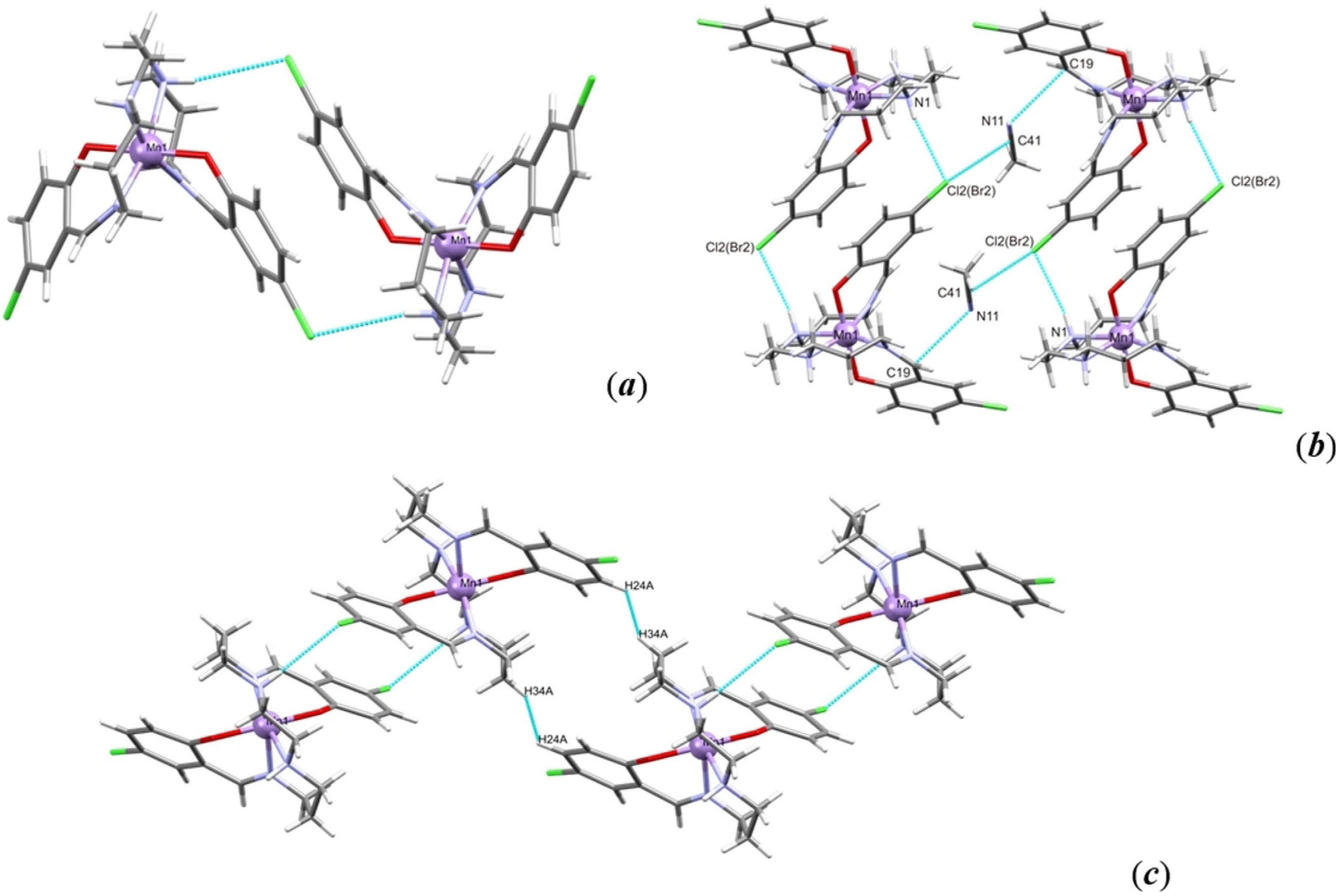

Figure 4. a) Hydrogen-bonded dimer of $[MnL1]^{+}$ cations in the crystal structure of **I**. b) Fragment of the crystal structure of **I** and **II**. c) H···H contacts in the cationic $[MnL1]^{+}$ layer of **I**. The dashed cyan lines show intermolecular contacts. Lengths of selected noncovalent contacts [Å]: a) All hydrogen-bond parameters are shown in Table 2; b) *d*(Cl2···C41) = 3.246, *d*(N11···C19) = 3.00 Å for **I**, *d*(Br2···C41) = 3.280, *d*(N11···C19) = 3.014 Å for **II**; c) *d*(H24A···H34A) = 2.28 Å for **I**, *d*(H24A···H34A) = 2.15 Å for **II**.

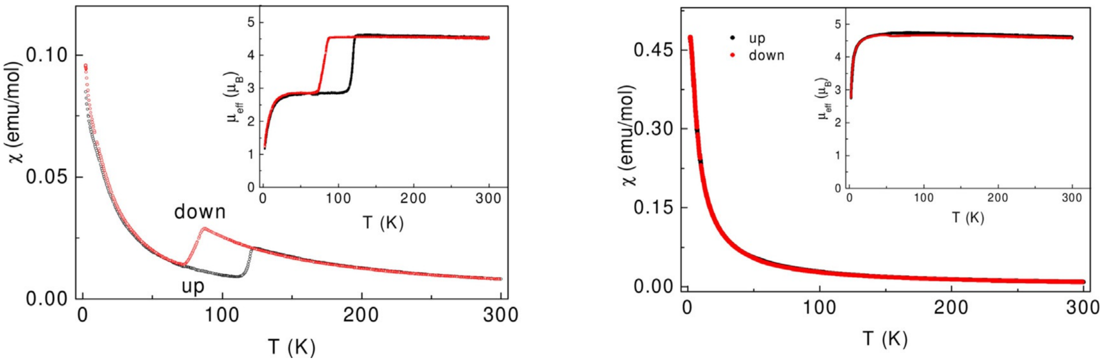

Figure 5. Temperature dependence of the magnetic susceptibility χ in **I** (left panel) and **II** (right panel) measured on both warming and cooling. Insets: the temperature dependence of the effective magnetic moments, proportional to the χT product.

Magnetic properties

The temperature dependencies of the magnetic susceptibility χ of **I** and **II** are shown in Figure 5. Very clearly, complex **I** exhibits a spin crossover that manifests itself as a sharp step-like anomaly in the dependence of χ versus T (left panel of Figure 5). The phase transition is associated with the switching of the spin state of Mn^{III} ($3d^4$) between high-spin ($S=2$) and low-spin ($S=1$) configurations. The values of the effective magnetic moments above and below the transition temperature were obtained by using the formula $\mu_{eff}=\sqrt{8\chi T}\mu_B$ and are equal to $4.61\mu_B$ and $2.83\mu_B$, respectively, as shown in the inset in the left panel of Figure 5. The experimental value above the spin crossover is lower than the value of $4.9\mu_B$ predicted for $S=2$, which could be due to the presence of the unquenched orbital contribution in the $3d^4$ ion. The experimental value below the spin crossover is consistent with that calculated for the LS state ($\mu_{eff}=2.83\mu_B$) assuming that the g factor equals 2. The radical-anionic subsystem does not contribute to the observed magnetic susceptibility, which is associated with the strong exchange interactions within $(TCNQ^{-\bullet})_2$ dimers that are present in the structure of the TCNQ stacks. Antiferromagnetic exchange interactions are characteristic of TCNQ salts with localized electron states.[25,26] The magnetic susceptibility recorded in cooling and warming modes revealed the hysteretic character of the transition in complex **I**, the multiple scans proving the reversibility of the hysteresis loop. The hysteresis window of 50 K is a record for d^4 SCO complexes. The wide hysteretic profile of the spin crossover indicates the cooperative behavior of the magnetic centers that may occur as a result of subtle balance of intermolecular interactions in crystals of **I**. The magnetic susceptibility of complex **II** does not show a spin-state transition in the temperature range of 2–300 K (right panel of Figure 5). The value of the effective magnetic moment calculated from the experimental data is $\mu_{eff}=4.6\mu_B$, which corresponds to the HS state ($S=2$) of Mn^{3+}, as shown in the inset to the right panel of Figure 5. At very low temperatures, a downward deviation of the χT product, that is, the effective magnetic moment μ_{eff}, is seen for both complexes. This behavior could be associated with zero-field splitting effects for the Mn^{3+} ion. The fundamental differences in the magnetic behavior of compounds **I** and **II** are probably associated with differences in the intermolecular interactions in the crystals of these compounds: Strong hydrogen bonding between cations and cations and anions in the crystals of **II** as compared with in the crystals of **I** likely prevents the spin transition in **II**.

In this regard, it should be noted that a strong correlation between supramolecular packing and spin crossover in cationic complexes of Mn^{III} with ligands of the sal-N-1,5,18,12 family has already been remarked in the literature.[13,14,18,20,21] In particular, the replacement of the AsF_6^- anion by SbF_6^- in the $[Mn(sal\text{-}1,5,8,12)]^+$ SCO complex led to close contacts between the phenyl groups of the ligands and as a result to suppression of spin transition.[21]

Extended X-ray absorption fine structure

The study of the magnetic properties of compound **I** clearly showed that on cooling it undergoes a spin crossover. Because X-ray studies at helium temperatures present some difficulties, we used the extended X-ray absorption fine structure (EXAFS) method to analyze the coordination polyhedron MnN_4O_2 after the spin transition. The investigations were carried out at the temperatures of 28 and 300 K on both compounds **I** and **II** (see the Experimental Section). The results of the EXAFS measurements allowed the bond lengths in the first coordination sphere of Mn^{III} to be determined (Figure 6 and Table 4). The data obtained for $[Mn(5\text{-}Br\text{-}sal\text{-}N\text{-}1,5,8,12)]TCNQ_{1.5}\cdot 2\,CH_3CN$ (**II**) can be used to evaluate the effects of thermal expansion, because no spin-state transition occurs in this compound. There are three types of ligand coordinating the Mn^{3+} ion within the MnN_4O_2 octahedron. The apical positions are taken by oxygen ions, whereas the basal positions are occupied by pairs of imine and amine nitrogen atoms. Evidently, both the apical and basal distances are sensitive to spin crossover, but the absolute values of the ligand displacements are most pronounced for the nitrogen atoms in the basal plane. This means that the spin-state transition should be associated with the occupation/deoccupation of the $d_{x^2-y^2}$ orbital belonging to the e_g orbital. In turn, this should lead to a decrease in the basal Mn–N bond lengths on going from the HS state to the LS state, as is observed in the case of compound **I** (Figure 6 and Table 4) and other similar Mn^{III} complexes described in the liter-

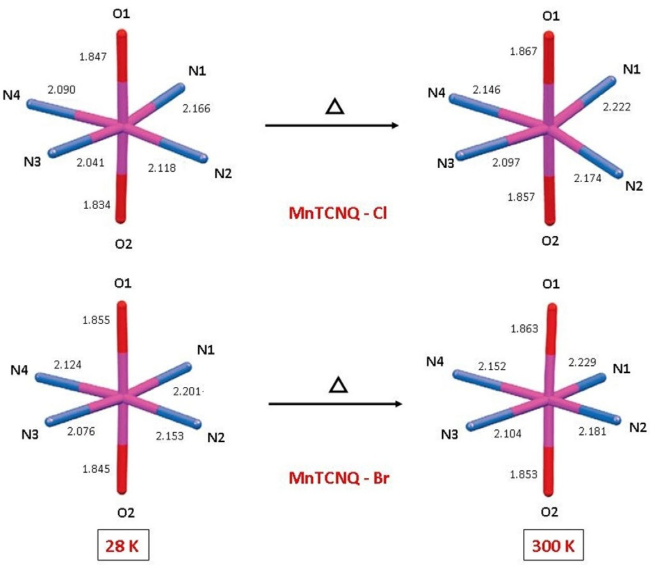

Figure 6. First coordination spheres of complexes **I** and **II** showing the changes in the Mn–ligand bond lengths upon warming.

ature.[21] Without thermal expansion effects, the average displacement over all six donor atoms upon spin crossover in **I** is 0.045, which is in line with the expected trend upon transition to $S=1$ in d^4 complexes.[11]

The thermal expansion effects constitute about one half of the displacement of the nitrogen atoms in the basal plane and about one third for the apical oxygen atoms. Quantitatively, the spin-crossover contribution to the ligand displacements is 0.012–0.015 Å for the oxygen atoms and 0.028 Å for the nitrogen atoms (see Table 4).

Conducting properties

The conductivity in the *ab* plane σ_a (along the TCNQ stacks, the *a* axis) at room temperature for six measured crystals of **I** was in the limits (0.9–1.6)$\times10^{-4}$ ohm^{-1}cm^{-1} and their anisotropy σ_a/σ_c was found to be in the range 28–60.

The error of about 40% in the resistivity calculations is mainly due to the fact that the shapes of the samples were far from ideal rectangular plates. The temperature dependence of the in-*ab*-plane resistance $R_{\parallel}$ (along the TCNQ stacks) for compound **I** is presented in Figure 7.

As seen from the inset in Figure 7, the sample resistance increases exponentially with the characteristic activation energy $\Delta=0.19$ eV as the temperature decreases. The Δ value for all the measured samples lies in the limits 0.19–0.21 eV. Upon cooling, the exponential increase in resistivity at given parameters prevents its overlap with the spin-crossover effect, which occurs at lower temperatures.

For four measured crystals of compound **II**, the conductivity along the TCNQ stacks amounted to (1.4–8.0)$\times10^{-4}$ ohm^{-1}cm^{-1} and the activation energy was in the same limits as for compound **I**. The conductivities at room temperature and activation energies for **I** and **II** are typical of radical-anion TCNQ salts with a cation/anion composition of 2:3 with localized electronic states in the TCNQ stacks.[27–29]

Table 4. Extended X-ray absorption fine structure (EXAFS) fitting results for **I** and **II** at 300 and 28 K (in parentheses).

Cmpd	Atom	Amp.[a]	$\sigma^{2[b]}$ [Å]	E_0[c] [eV]	$R_{initial}$[d] [Å]	ΔR [Å]	$R_{fitting}$[e] [Å]	Shift[f] [Å]
I (Cl)	O	0.538 (0.523)	0.002 (0.001)	−0.986 (−6.055)	1.871	−0.014 (−0.037)	1.857 (1.834)	0.023
					1.871		1.867 (1.847)	0.020
	N	0.968 (0.916)	0.013 (0.016)		2.095	0.002 (−0.054)	2.097 (2.041)	0.056
					2.144		2.146 (2.090)	0.056
					2.172		2.174 (2.118)	0.056
					2.220		2.222 (2.166)	0.056
II (Br)	O	0.661 (0.630)	0.002 (0.001)	−0.081 (−1.572)	1.871	−0.018 (−0.026)	1.853 (1.845)	0.008
					1.881		1.863 (1.855)	0.008
	N	0.946 (0.792)	0.013 (0.016)		2.095	0.009 (−0.019)	2.104 (2.076)	0.028
					2.144		2.152 (2.124)	0.028
					2.172		2.181 (2.153)	0.028
					2.220		2.229 (2.201)	0.028

[a] Coordinate number = degenerate atom × Amp. [b] σ is the Debye–Waller factor (disorder in the arrangement of atoms). [c] E_0 is the energy shift parameter used to align the theoretical calculated spectrum to the energy grid of the measured spectrum. [d] $R_{initial}$ is the initial bond length determined from the XRD data. [e] $R_{fitting}$ is the bond length after fitting ($R_{fitting}=R_{initial}+\Delta R$). [f] The shift is the difference between the values at 300 and 28 K.

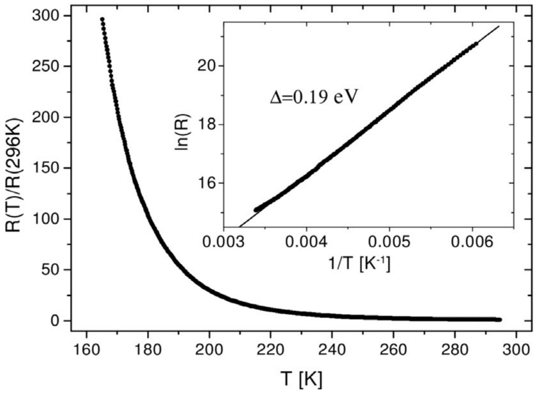

Figure 7. Temperature dependence of the in-*ab*-plane normalized resistance $R_{\|}$ (along the TCNQ stacks) for a crystal of compound **I**. Inset: Arrhenius plot demonstrating the exponential $R_{\|}(T)$ dependence.

Conclusions

To synthesize conducting spin-crossover compounds based on Mn^{III} complexes with ligands of the sal-N-1,5,8,12 family, the electroactive anion of TCNQ was used for the first time as the counter ion in these complexes. As a result, the compounds $[Mn(5\text{-}Cl\text{-}sal\text{-}N\text{-}1,5,8,12)]TCNQ_{1.5}\cdot 2\,CH_3CN$ (**I**) and $[Mn(5\text{-}Br\text{-}sal\text{-}N\text{-}1,5,8,12)]TCNQ_{1.5}\cdot 2\,CH_3CN$ (**II**) were obtained and showed semiconducting behavior. Magnetic measurements and variable-temperature X-ray and EXAFS analyses revealed an abrupt hysteretic phase transition in **I** associated with a crossover between the low-spin ($S=1$) and high-spin ($S=2$) states of Mn^{III} and changes in bond lengths within the MnN_4O_2 octahedra. Unlike **I**, complex **II**, which is isomorphic with **I**, evidences no spin-crossover phenomena. It is known that supramolecular aspects in mononuclear Mn^{III} SCO complexes associated with intermolecular hydrogen bonding and π–π stacking interactions between phenyl groups in the ligands greatly influence the magnetic properties of these compounds.[21] The wide hysteretic profile of the spin crossover in **I** indicates the cooperative behavior of the magnetic centers that may occur as a result of a subtle balance of the hydrogen bonds between cations and cations and anions in the crystals of **I**. The intermolecular hydrogen bonding in the crystal lattice of **II** is stronger than in **I**, which probably leads to suppression of the spin transition in **II**. It is necessary, however, to point out another possible reason for the different magnetic behavior of complexes **I** and **II**. Essentially, the spin crossover in coordination compounds is driven by the increase in entropy ΔS in the transition from the LS to HS state. This change is due to both the lower electronic degeneracy ΔS_e and lower vibrational frequencies ΔS_v of the high-spin state. In fact, the total entropy change is dominated by the vibrational contribution.[30] In terms of the dynamic theory of the crystal lattice, the spin crossover is a vibronic transition driven by the stretching vibrations of the metal–ligand bonds in the environment of the central ion. In the case of the title compounds, these are Mn–N vibrations that switch the system between distinctly different electronic configurations.

The anharmonicity of the crystal lattice plays an important role in the spin crossover.[31] The bending vibrations of adjusting units may or may not enhance the anharmonicity of the stretching vibrations.[32] The only molecular difference between compounds **I** and **II** concerns the mass of the halogen ions terminating the nitrogen–carbon–halogen (N–C–Hal) units. This results in different frequencies of the N–C–Hal vibrations. The spin crossover in **I** must be assigned to a mode that has mixed character due to the overlap of Mn–N stretching vibrations and N–C–Cl bending vibrations. Evidently, the overlap between N–C–Br bending and Mn–N stretching modes is not that strong in **II**, being unable to assist the spin crossover. The measurements of the temperature-dependent nuclear inelastic scattering of synchrotron radiation may clarify these issues. Complexes **I** and **II** are useful models for further experimental investigations of the microscopic origins of spin-crossover phenomena. The molecular and crystalline engineering described in this work provides useful information for the design of new conducting Mn^{III} SCO complexes in which one can expect the coexistence of conductivity and spin crossover in the same temperature range.

Experimental Section

Synthesis

Commercial solvents were used without further purification unless otherwise specified. Reactants commercially obtained: 5-chlorosalicylaldehyde, 5-bromosalicylaldehyde, *N*,*N*′-bis(3-aminopropyl)ethylenediamine, manganese perchlorate ($Mn(ClO_4)_2\cdot 6H_2O$), lithium iodide (LiI), and 7,7,8,8-tetracyanoquinodimethane were purchased from Sigma–Aldrich. The complexes $[Mn(5\text{-}Cl\text{-}sal\text{-}N\text{-}1,5,8,12)]ClO_4$, $[Mn(5\text{-}Br\text{-}sal\text{-}N\text{-}1,5,8,12)]ClO_4$, and LiTCNQ were prepared according to procedures reported in the literature.[27,33]

$[Mn(5\text{-}Cl\text{-}sal\text{-}N\text{-}1,5,8,12)]TCNQ_{1.5}\cdot 2\,CH_3CN$ (I): A hot filtered solution of $[Mn(5\text{-}Cl\text{-}sal\text{-}N\text{-}1,5,8,12)]ClO_4$ (121 mg, 0.2 mmol) in acetonitrile (10 mL) was added to a hot solution of LiTCNQ (41 mg, 0.2 mmol) and TCNQ (40 mg, 0.2 mmol) in acetonitrile (20 mL) under an atmosphere of argon. The reaction mixture was cooled to −5 °C in a refrigerator overnight. Black plate-like crystals were collected by filtration, washed with cold acetonitrile and diethyl ether, and dried in air. Yield: 70%; elemental analysis calcd (%) for $C_{44}H_{38}Cl_2MnN_{12}O_2$: C 59.19, H 4.26, N 18.83; found: C 59.35, H 4.12, N 18.68.

$[Mn(5\text{-}Br\text{-}sal\text{-}N\text{-}1,5,8,12)]TCNQ_{1.5}\cdot 2\,CH_3CN$ (II): Crystals of **II** were obtained by a similar method using $[Mn(5\text{-}Br\text{-}sal\text{-}N\text{-}1,5,8,12)]ClO_4$. Yield: 70%; elemental analysis calcd (%) for $C_{44}H_{38}Br_2MnN_{12}O_2$: C 53.92, H 3.48, N 17.03; found: C 53.82, H 3.87, N 17.13.

X-ray crystallography

X-ray diffraction data for single crystals of **I** (at 100 and 220 K) and **II** (at 100 K) were collected on a Agilent XCalibur CCD diffractometer equipped with an EOS detector (Agilent Technologies UK Ltd, Yarnton, Oxfordshire, England) using graphite-monochromated $Mo_{K\alpha}$ radiation ($\lambda = 0.71073$ Å). The structures were solved by direct methods and refined against all F^2 data.[34] All non-hydrogen atoms were refined by using anisotropic thermal parameters. The positions of hydrogen atoms were obtained from difference Fourier synthesis and refined with riding model constraints. Selected crystallographic parameters and details of data collection and refinement are given in Table S2 in the Supporting Information.

CCDC 1895355, 1895356, and 1895357 contain the supplementary crystallographic data for this paper. These data are provided free of charge by The Cambridge Crystallographic Data Centre.

Physical measurements

Thermogravimetric analysis was performed in an argon atmosphere at a heating rate of 5.0 °C min^{-1} using a NETZSCH STA 409 C Luxx thermal analyzer interfaced to a QMS 403 Aelos mass spectrometer.

The magnetic measurements were performed on freshly filtered polycrystalline samples of compounds **I** and **II** in the temperature range of 2–300 K using the vibrating sample magnetometer (VSM) option of the "Quantum Design" Physical Properties Measurements System PPMS-9T. The measurements were performed at a scan rate of 1 K min^{-1} in an applied magnetic field of 0.1 T. The data were corrected for diamagnetic contributions calculated as the sum of Pascal's constants.

The temperature dependence of the electrical resistance of single crystals was measured by means of a four-probe technique using a multimeter with high input impedance. The measurements were carried out in the Montgomery geometry: Two contacts were attached to each of two opposite sample surfaces with a conducting graphite paste. The room-temperature resistivity and sample anisotropy were calculated from the measured in-*ab*-plane $R_{\parallel}$ (along the TCNQ stacks, the *a* axis) and out-of-plane $R_{\perp}$ (along the *c* axis) resistances by using the well-known mathematical procedure.[35,36] In the control experiments, we measured the in-plane resistance by using a two-probe geometry, and we found that the result did not differ considerably from that obtained by using the four-probe geometry, that is, the contact resistance was of the same order or even smaller than the resistance of the samples.

The Mn K-edge spectra (6540 eV) were measured at room temperature at the 17C beamline of the National Synchrotron Radiation Research Center in Taiwan. The fluorescence mode was employed with a beam incidence of 45° with respect to the sample plane and the signal was measured by using a Lytle detector. A double crystal Si(111) monochromator was used, so that the measured energy resolution was better than 1.4 eV. The EXAFS spectra were obtained by background subtraction of the XAS data $\mu(E)$ and the conversion of $\mu(E)$ into $\chi(k)$ by means of ATHENA.[37] After that, we Fourier-transformed (FT) the spectra of $\chi(k)$ by using the Hanning windows with k ranging from 1.081 to 2.168 Å^{-1} and k^3 weighting. In doing so, the FT spectra (see Figures S4–S7 in the Supporting Information) of the Mn *K*-edge with the *R*-space information of bond length was plotted. In the spectra, there are two main peaks for compounds **I** and **II**, with each peak corresponding to the Mn–O bond and Mn–N bond from left to right. Next, the fitting was carried out by using ARTEMIS[37] with the amplitude, Debye–Waller factor, energy shift, and bond length shift used as fitting parameters. By using the bond-length fit in ARTEMIS, we constructed the coordination spheres of compounds **I** and **II** by loading the values in GAUSSVIEW, followed by optimization to visualize the local structure.

Acknowledgements

This work was carried out within the state assignment (no 0089-2019-0011) for the IPCP RAS. We acknowledge support from the Ministry of Education and Science of the Russian Federation within the framework of Increase Competitiveness Program of NUST "MISiS" (Grant No. K2-2017-084; by Act 211 of the Government of Russian Federation, Contracts No. 02.A03.21.0004 and No. 02.A03.21.0011). D.V.K. and G.V.S. acknowledge the Ministry of Science and Higher Education of the Russian Federation (Agreement no. 14.W03.31.0001). This work was also supported by the Joint Russia–Taiwanese project of the Russian Foundation for Basic Research (No. 18-52-52005) and of Taiwan MOST (No. 107-2923-M-009-001-MY3). J.-Y.L. was also supported by the Center for Emergent Functional Matter Science of National Chiao Tung University through The Featured Areas Research Center Program and the Research Team of Photonic Technologies and Intelligent Systems at NCTU within the framework of the Higher Education Sprout Project of the Ministry of Education (MOE) in Taiwan. The work was also supported by the projects of the Russian Foundation for Basic Research (No. 18-32-00153 and 18-02-00280).

Conflict of interest

The authors declare no conflict of interest.

Keywords: conducting materials · EXAFS spectroscopy · magnetic properties · polyfunctional materials · X-ray diffraction

[1] *Spin Crossover in Transition Metal Compounds I* (Eds.: P. Gütlich, H. A. Goodwin), Springer, Berlin, **2004**, pp. 1–324.
[2] *Spin-Crossover Materials: Properties and Applications* (Ed.: M. A. Halcrow), Wiley, Oxford, **2013**, pp. 1–564.
[3] S. Brooker, *Chem. Soc. Rev.* **2015**, *44*, 2880–2892.
[4] M. A. Senarís-Rodríguez, J. B. Goodenough, *J. Solid State Chem.* **1995**, *116*, 224–231.
[5] O. Sato, Z.-Y. Li, Z.-Sh. Yao, S. Kang, S. Kanegawa in *Spin-Crossover Materials: Properties and Applications* (Ed.: M. A. Halcrow), Wiley, Oxford, **2013**, pp. 303–319.
[6] Y. N. Shvachko, D. V. Starichenko, A. V. Korolyov, A. I. Kotov, L. I. Buravov, V. N. Zverev, S. V. Simonov, L. V. Zorina, E. B. Yagubskii, *Magnetochemistry* **2017**, *3*, 9.
[7] Yu. N. Shvachko, D. V. Starichenko, A. V. Korolyov, E. B. Yagubskii, A. I. Kotov, L. I. Buravov, K. A. Lyssenko, V. N. Zverev, S. V. Simonov, L. V. Zorina, O. G. Shakirova, L. G. Lavrenova, *Inorg. Chem.* **2016**, *55*, 9121–9130.
[8] M. Nakano, N. Fujita, G. E. Matsubayashi, W. Mori, *Mol. Cryst. Liq. Cryst.* **2002**, *379*, 365–370.
[9] H. Phan, S. M. Benjamin, E. Steven, J. S. Brooks, M. Shatruk, *Angew. Chem. Int. Ed.* **2015**, *54*, 823–827; *Angew. Chem.* **2015**, *127*, 837–841.
[10] X. Zhang, Z.-X. Wang, H. Xie, M.-X. Li, T. J. Woods, K. R. Dunbar, *Chem. Sci.* **2016**, *7*, 1569–1574.
[11] G. G. Morgan, K. D. Murnaghan, H. Müller-Bunz, V. McKee, Ch.J. Harding, *Angew. Chem. Int. Ed.* **2006**, *45*, 7192–7195; *Angew. Chem.* **2006**, *118*, 7350–7353.
[12] S. Wang, M. Ferbinteanu, C. Marinescu, A. Dobrinescu, Q.-D. Ling, W. Huang, *Inorg. Chem.* **2010**, *49*, 9839–9851.
[13] K. Pandurangan, B. Gildea, C. Murray, C. J. Harding, H. Müller-Bunz, G. G. Morgan, *Chem. Eur. J.* **2012**, *18*, 2021–2029.
[14] B. Gildea, L. C. Gavin, C. A. Murray, H. Müller-Bunz, C. J. Harding, G. G. Morgan, *Supramol. Chem.* **2012**, *24*, 641–653.
[15] P. N. Martinho, B. Gildea, M. M. Harris, T. Lemma, A. D. Naik, H. Müller-Bunz, T. E. Keyes, Y. Garcia, G. G. Morgan, *Angew. Chem. Int. Ed.* **2012**, *51*, 12597–11260; *Angew. Chem.* **2012**, *124*, 12765–12769.
[16] S. Wang, W. R. He, M. Ferbinteanu, Y. H. Li, W. Huang, *Polyhedron* **2013**, *52*, 1199–1205.

[17] Y. Chen, F. Gao, R.-M. Wei, Y. Zhang, Y.-Q. Zhang, Y. Song, *Dalton Trans.* **2014**, *43*, 3783 – 3791.
[18] S. Wang, Y.-H. Li, W. Huang, *Eur. J. Inorg. Chem.* **2015**, 2237 – 2244.
[19] A. J. Fitzpatrick, E. Trzop, H. Müller-Bunz, M. M. Dirtu, Y. Garcia, E. Collet, G. G. Morgan, *Chem. Commun.* **2015**, *51*, 17540 – 17543.
[20] S. Wang, W.-T. Xu, W.-R. He, S. Takaishi, Y.-H. Li, M. Yamashita, W. Huang, *Dalton Trans.* **2016**, *45*, 5676 – 5688.
[21] S. Wang, Y.-J. Li, F.-F. Ju, W.-T. Xu, K. Kagesawa, Y.-H. Li, M. Yamashita, W. Huang, *Dalton Trans.* **2017**, *46*, 11063 – 11077 and references therein.
[22] H. Miyasaka, A. Saiton, S. Abe, *Coord. Chem. Rev.* **2007**, *251*, 2622 – 2664.
[23] A. Bousseksou, G. Molnar, L. Salmon, W. Nicolazzi, *Chem. Soc. Rev.* **2011**, *40*, 3313 – 3335.
[24] T. J. Kistenmacher, T. J. Emge, A. N. Bloch, D. O. Cowan, *Acta Crystallogr. Sect. B* **1982**, *38*, 1193 – 1199.
[25] R. G. Kepler, *J. Chem. Phys.* **1963**, *39*, 3528 – 3532.
[26] I. F. Shchegolev, *Phys. Status Solidi A* **1972**, *12*, 9 – 45.
[27] L. Melby, R. Harder, W. Hertler, W. Mahler, R. Benson, W. Mochel, *J. Am. Chem. Soc.* **1962**, *84*, 3374.
[28] W. J. Siemons, P. E. Bierstedt, R. G. Kepler, *J. Chem. Phys.* **1963**, *39*, 3523.
[29] R. P. Shibaeva, L. O. Atovmyan, *J. Struct. Chem.* **1972**, *13*, 514 – 531.
[30] A. Bousseksou, J. J. McGarvey, F. Varret, J. A. Real, J.-P. Tuchagues, A. C. Dennis, M. L. Boillot, *Chem. Phys. Lett.* **2000**, *318*, 409 – 416.
[31] V. V. Shelest, A. V. Khristov, G. G. Levchenko, *Low Temp. Phys.* **2016**, *42*, 505 – 512.
[32] A. X. Trautwein, H. Paulsen, H. Winkler, H. Giefers, G. Wortmann, H. Toftlund, J. A. Wolny, A. I. Chumakov, O. Leupold, *J. Phys. Conf. Ser.* **2010**, *217*, 012125.
[33] A. Panja, N. Shaikh, S. Gupta, R. Butcher, P. Banerjee, *Eur. J. Inorg. Chem.* **2003**, 1540.
[34] G. M. Sheldrick, *SHELXTL v. 6.14*, *Structure Determination Software Suite*; Bruker AXS: Madison, Wisconsin, USA, **2000**.
[35] H. C. Montgomery, *J. Appl. Phys.* **1971**, *42*, 2971.
[36] L. I. Buravov, *Sov. Phys. Tech. Phys.* **1989**, *34*, 464.
[37] B. Ravel, M. Newville, *J. Synchrotron Radiat.* **2005**, *12*, 537 – 541.

Manuscript received: April 17, 2019
Revised manuscript received: May 28, 2019
Accepted manuscript online: May 30, 2019
Version of record online: July 4, 2019